Shock wave-boundary layer interaction in a transitional flow over a backward-facing step

Hu, Weibo; Hickel, Stefan; van Oudheusden, Bas

Important note
To cite this publication, please use the final published version (if applicable).
Please check the document version above.

SHOCK WAVE-BOUNDARY LAYER INTERACTION IN A TRANSITIONAL FLOW OVER A BACKWARD-FACING STEP

Weibo Hu[(1)], Stefan Hickel[(2)] and Bas van Oudheusden[(3)]

Faculty of Aerospace Engineering, Delft University of Technology
Kluyverweg 2, 2629HS, Delft, The Netherlands
[(1)]*W.Hu-2@tudelft.nl,* [(2)]*S.Hickel@tudelft.nl,* [(3)]*B.W.vanOudheusden@tudelft.nl*

ABSTRACT

The unsteadiness of shock wave-boundary layer interactions is investigated in a transitional backward-facing step flow at $Ma = 1.7$ and $Re_{\delta_0} = 13718$ using large eddy simulation. The mean and instantaneous flow shows that the laminar inflow undergoes a laminar-to-turbulence transition in which Kelvin-Helmholtz vortices form, distort and eventually break down into small hairpin-like vortices. The interaction system features broadband frequency oscillations in a range $f\delta_0/u_\infty = 0.03 \sim 0.23$ based on the spectral and statistical analysis. The results of dynamic mode decomposition indicate that the medium-frequency motions centered at $f\delta_0/u_\infty = 0.06$ are related to the shock winkling and the shedding of large coherent vortices, while the lower (centered at $f\delta_0/u_\infty \approx 0.01$) and higher ($f\delta_0/u_\infty \approx 0.1$) frequency unsteadiness is associated with the periodical dilatation and shrinking of separation system and the convection of upstream K-H vortices respectively.

1. INTRODUCTION

Shock wave-boundary layer interaction (SWBLI) has been an active topic in the development of transonic/supersonic aircraft and rockets due to their ubiquity in different systems of these high speed vehicles, including supersonic inlets, over-expanded nozzles, high-speed airfoils and other discontinuous geometries [4, 7]. In most cases, SWBLI leads to considerable detrimental and potentially hazardous effects on the performance of vehicles. In external flows, SWBLI can induce increasing flight drag and intense localized thermal and mechanical loads. In terms of internal flows, it may produce pressure loss and inflow distortion, or even the unstart of the inlet,

which is not uncommon to occur in scramjets. In addition, SWBLI is often accompanied with low-frequency unsteadiness of shock waves whose frequency is typically two orders smaller than the characteristic frequency of the incoming boundary layer [2]. These large-scale low-frequency unsteady motions can result in material failure and impaired structural integrity of aircraft.

Understanding the origin of the unsteadiness is a major research topic in the domain of SWBLI. In general, there are mainly two opinions about the origin of this unsteady behavior, categorized as upstream and downstream dynamics [5, 19]. The first theory associates the unsteady motion with the fluctuations from the upstream turbulent boundary layer. The other category attributes these oscillations to the dynamics of the separation bubble. However, most of the existing efforts have been put on the incident shock and compression ramp interactions. In the current work, we consider the unsteadiness of SWBLI in the (transitional) flow over a backward-facing step (BFS).

2. FLOW CONFIGURATION AND NUMERICAL SETUP

2.1 Flow configuration

For the present study, the test case is an open BFS (i.e., without a upper wall) with a supersonic laminar boundary layer as inlet condition. The flow configuration is similar to the recent experimental works of Zhu *et al.*[31], a schematic of which is shown in Fig. 1.

The laminar inflow is characterized by a free stream with $Ma = 1.7$ and $Re_{\delta_0} = 13718$ based on the reference boundary layer thickness δ_0 at the inlet. Main flow parameters are summarized in Tab. 1. The variables represent free stream flow parameters with subscript ∞ and
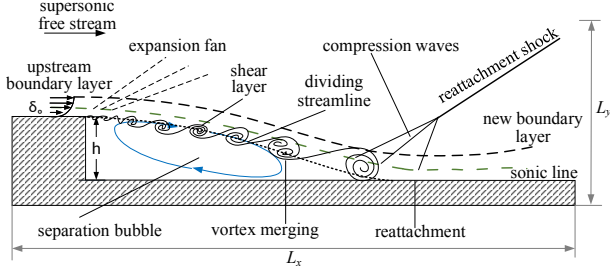
Figure 1: Schematic of the computational flow domain with main flow features (not in scale).

stagnation parameters with subscript 0 respectively.

Table 1: Main flow parameters of the current case

Ma_∞	U_∞	δ_0	Re_∞
1.7	469.85 m/s	1 mm	$1.3718 \times 10^7 \, \mathrm{m}^{-1}$

T_0	p_0	h	p_∞
300 K	1×10^5 Pa	3 mm	20 259 Pa

2.2 Numerical setup

The size of the computational domain is $[L_x, \ L_y, \ L_z] = [110\delta_0, \ 33\delta_0, \ 5\delta_0]$ with a length of $40\,\delta_0$ upstream of the step in order to allow uncertain effects from the inlet boundary layer to vanish. The height of the step is three times larger than the inlet boundary layer thickness.

We employ the implicit large eddy simulation (ILES) method of Hickel *et al.* [11] for solving the compressible Navier-Stokes equations. In this solver, the subgrid scale model is fully merged into the numerical scheme provided by the adaptive local deconvolution method (ALDM). The viscous flux is discretized by a second-order central difference scheme and time marching is achieved by an explicit third-order total variation diminishing (TVD) Runge-Kutta scheme [6]. This code has been successfully applied to various supersonic flow cases, including SWBLI on a compression ramp [8] and flat plate [19], transition between regular and irregular shock patterns [16]. More details about this ILES method can be found in Hickel *et al.* [11, 10].

For the spatial discretization, a cartesian grid structure with block-based local refinement was applied for the entire domain, as displayed in Fig. 2. In addition, a hyperbolic gird stretching strategy was used in the wall-normal direction at the region downstream of the step. Upstream of the step, the near wall grids are distributed uniformly to keep mesh consistency across blocks upstream and downstream of the step. In addition, they are all refined near the wall to ensure a well-resolved wall shear stress. The grid spacing becomes coarser with increasing wall distance but the expansion ratio is not larger than two to

ensure a good smoothness of the grid stretching. Using this discretization strategy, the computation domain has around 8.47×10^6 cells; thus we obtain a spatial resolution of the flow field with $\Delta x_{min}^+ \times \Delta y_{min}^+ \times \Delta z^+ = 0.9 \times 1.0 \times 20$ for the whole domain. The temporal resolution, that is the time step, is around $\Delta t u_\infty / \delta_0 = 7.6 \times 10^{-4}$.
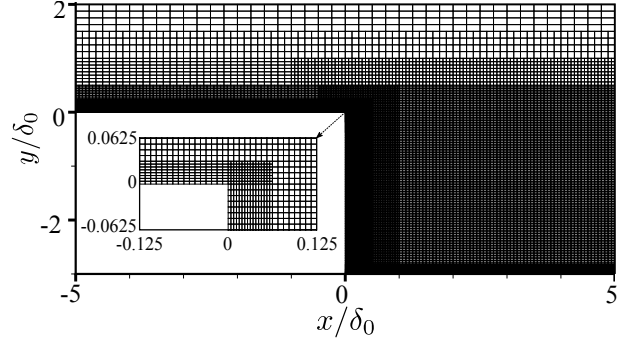

Figure 2: Grid distribution in the x-y plane in the computational domain around the step.

At the domain inlet, a clean compressible laminar boundary layer profile is imposed. The step and wall are modeled as non-slip adiabatic surfaces. All the flow variables are extrapolated at the outlet of the domain. On the top of the domain, non-reflecting boundary conditions based on Riemann invariants are used. Periodic boundary conditions are imposed in the spanwise direction.

3. RESULTS

3.1 Mean and instantaneous flow organization

The main flow features are illustrated by the time- and spanwise-averaged density contour, shown in Fig. 3. The incoming laminar flow experiences a centered Prandtl-Meyer expansion and separates at the fixed separation point (step corner) due to the sudden geometry expansion. Then the free shear layer develops towards the downstream wall and finally impinges on the wall surface. Compression waves are generated around the reattachment location, which coalesce into a reattachment shock. The low-speed recirculating flow forms a separation bubble underneath the dividing line (isoline of $u = 0$), while the high-speed flow proceeds downstream by overcoming the slight pressure rise. The mean reattachment length is about $L_r = 10.9\delta_0$ ($3.6h$), which is consistent with existing results, reporting that the reattachment length is usually within $3.0 \sim 4.0h$ around the current Mach number [13, 15].

The separation length is further confirmed by the mean skin friction $\langle C_f \rangle$ distribution in Fig. 4a, where $\langle C_f \rangle$ is the skin friction normalized by $0.5\rho U_\infty^2$. The intensity of the reverse flow is not uniform in terms of $\langle C_f \rangle$ varying with
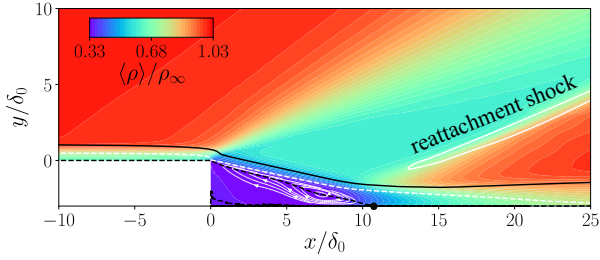
Figure 3: Time and spanwise-averaged density contours. A solid circle (•) indicates the reattachment point. The white dashed and solid line denote the isolines of $Ma = 1.0$ and $|\nabla p|\delta_0/p_\infty = 0.24$. The black dashed and solid line signify isolines of $u = 0.0$ and $u/u_e = 0.99$.

streamwise distance along the separation bubble. The level of $\langle C_f \rangle$ remains almost zero in the upstream part of the separation bubble ($0 < x/\delta_0 < 6.3$), which is followed by a decrease of $\langle C_f \rangle$ towards a global minimum at $x/\delta_0 = 8.4$. Then $\langle C_f \rangle$ slowly climbs up and eventually stays steady at around $\langle C_f \rangle = 2.6 \cdot 10^{-3}$ at $x/\delta_0 > 25$. The trend and level of $\langle C_f \rangle$ match well with the numerical results of Spazzini *et al.* [27] despite the different inlet boundary conditions and reattachment length. As will be shown later, this structure of $\langle C_f \rangle$ inside the recirculating region appears to be related to the low-frequency unsteadiness.

The wall pressure in Fig. 4b shows a sharp drop by about 50% in front of the step. The wall pressure then gradually reduces to its global minimum at $x/\delta_0 = 7.3$ in the separation bubble. In terms of the trend and variation, our results are in agreement with the numerical works of Karimi *et al.* [13]. We believe that these three inflection points of the wall-pressure distribution are related to the separation, onset of reattaching and reattachment respectively, as reported in [3].
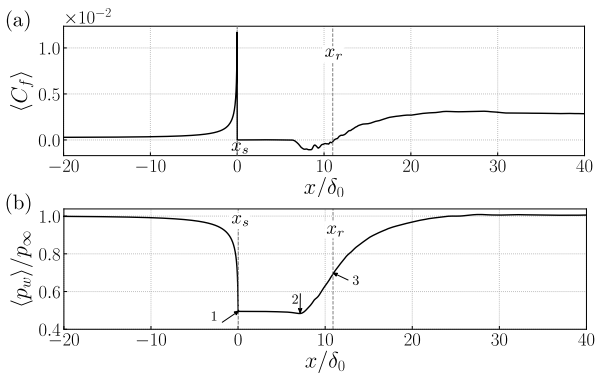

Figure 4: Time- and spanwise-averaged (a) skin friction and (b) wall pressure. The dash line indicates the averaged reattachment location

The vortical structures are visualized by the λ_2 vor-

tex criterion in Fig. 5. The large spanwise vortices are induced by the K-H instability. These K-H vortices are deforming continuously as a result of their secondary instability triggered by small horseshoe-like vortices below as the free shear layer flow develops downstream. The distorted vortices pair with each other and break down into several small Λ-shaped vortices in the reattaching event. Then they roll up and develop into larger hairpin vortices. The separated shear layer flow is featured with the formation of large-scale vortices via K-H instability, pairing process and break down as the shear layer evolves, similar as reported by Schäfer *et al.* [24] for their incompressible case. The vortex topology of the streamwise vortices below K-H vortices is also observed by the experimental [28] and numerical results [29] of a micro vortex generator.
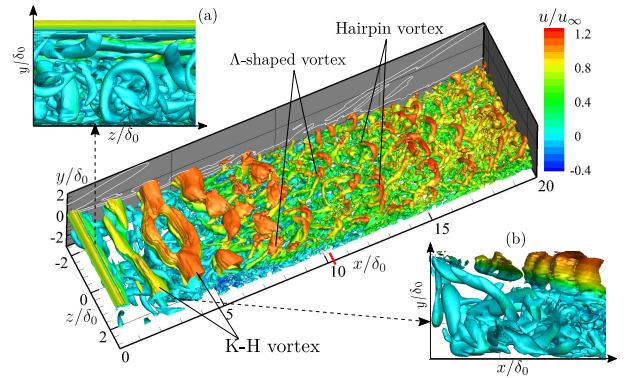

Figure 5: Instantaneous vortical structures at $tu_\infty/\delta_0 = 790.5$, visualized by isosurfaces of $\lambda_2 = -0.005$. The white line represents the isolines of $|\nabla p|\delta_0/p_\infty = 0.24$ at the slice $z/\delta_0 = -2.5$. The red solid line signifies the instantaneous spanwise-averaged reattachment point. The white arrow lines denote the streamlines in the separation bubble. (a) the ejection behavior; (b) the streamwise vortices

3.2 Spectral Analysis

The unsteadiness of the flow field can be examined by means of the frequency weighted power spectral density (FWPSD) of the pressure along the dividing line. Note that all the values of FWPSD have been normalized by the local integral values $\int P(f)\mathrm{d}f$ in order to better highlight the relative contributions at different frequencies, independent of the overall fluctuation strength. As we can see in Fig. 6, the separated flow features a low-frequency oscillation with $f\delta_0/u_\infty \approx 0.02$ right behind the step ($0 < x/\delta_0 < 1$). This unsteady behavior is believed to be associated with the breathing motion of the separation bubble, as we will discuss in the following section. The dominant frequency then shifts towards higher values of around $f\delta_0/u_\infty \approx 0.2$ where the oblique K-H

vortices are observed. As the shear layer develops, the energetic content of the shear layer gradually shifts to lower frequencies, which displays a broadband frequency spectrum from the low to high frequency ($4 < x/\delta_0 < 10.9$). Downstream of the reattachment location ($x/\delta_0 \geq 10.9$), the fluctuations of the boundary layer are randomly distributed over the spectrum without a clear preferred frequency.
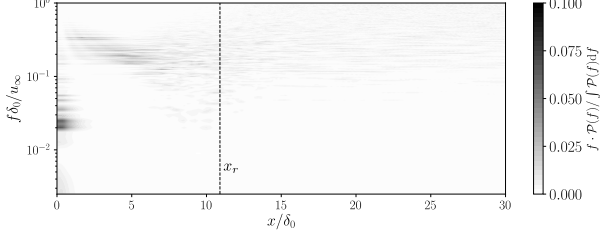

Figure 6: Frequency weighted power spectral density map of pressure signals along the dividing line based on $z = 0$ slice. The weighted spectra are normalized by $\int P(f)\mathrm{d}f$ at every streamwise location.

Time signals of three typical flow parameters are shown in Fig. 7 to further characterize the unsteady behavior of the separation system, including the spanwise-averaged reattachment point x_r, shock angle x_a and area of separation bubble x_b. The value of x_r is the first point with $u = 0.0$ on the first cell from the wall between $x/\delta_0 = 8.5$ and 13.5 based on the spanwise-averaged slice. The shock angle x_a is the angle between the positive x-direction and reattachment shock, which is defined by the isolines of $|\nabla p|\delta_0/p_\infty = 0.24$, and x_b is the area of the zone between the dividing line and wall. These temporal signals are extracted within time ranges $tu_\infty/\delta_0 = 600 \sim 1000$ with a sampling frequency $f_s\delta_0/u_\infty = 2$ as the non-dimensional frequency above the characteristic frequency of the turbulent integral scales u_∞/δ_0 is not of current interest. Their unsteadiness appears a modulation of broadband frequency scales because all the plots are irregular and aperiodic. The curve of the reattachment point has an almost vertical drop when it moves upstream, for example at around $tu_\infty/\delta_0 = 694$, which suggests that it moves upstream at a constant speed. When the reattachment location shifts downstream, it experiences a rapid relaxation. This sawtooth-like trajectory of the reattachment point is also reported in direct numerical simulation (DNS) results of a compression ramp by Priebe & Martin [21]. On the other hand, the falling of shock angle is smoother, without such strong sawtooth-like behavior. The passage of large-scale vortex in the shear layer and their shedding into the downstream flow contributes to the sawtooth-like motions [14, 17]. In terms of separation bubble, its temporal behavior seems more periodical, with the absence of many short-period fluctuations.

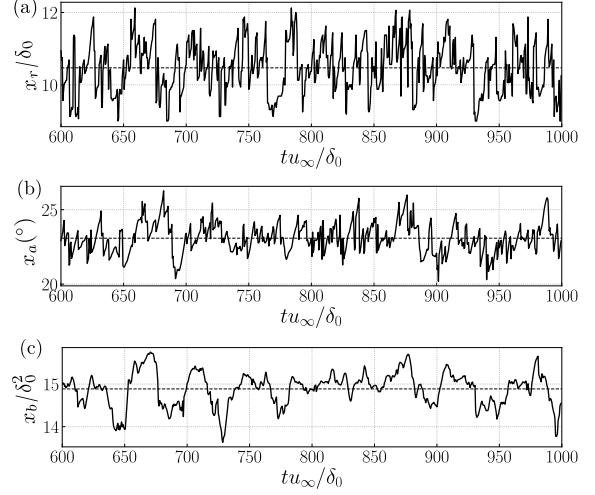The FWPSD of these signals is provided to analyze the

Figure 7: Temporal variation of (a) the reattachment point x_r, (b) shock angle x_a and (c) area of the separation bubble x_b. The dashed line denotes the mean value.

present leading frequency in more details, as shown in Fig. 8. The spectra of reattachment and shock angle both have three narrowband peaks around $f\delta_0/u_\infty = 0.02, 0.06$ and near 0.1. For the reattachment point position (solid line), most of the energy is contained at $f\delta_0/u_\infty = 0.2$, near the characteristic frequency of the K-H vortices. As for the shock angle (dashed line), the spectrum peaks are located around $f\delta_0/u_\infty = 0.02$ and 0.06, while the oscillation of the separation bubble has a single dominant frequency peak at $f\delta_0/u_\infty \approx 0.02$ (dotted line), which is two orders of magnitude lower than the characteristic frequency of the energetic turbulent scales u_∞/δ_0, in agreement with the widely reported low-frequency unsteadiness in SWBLI [22, 9].
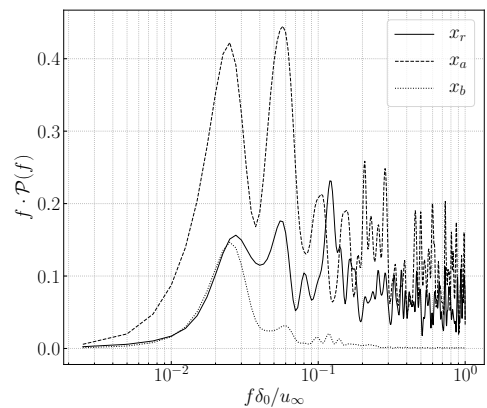

Figure 8: Frequency weighted power spectral density of the reattachment point x_r, shock angle x_a and area of the separation bubble x_b.

3.3 Statistical Analysis

There exist three distinct dominant frequencies of the unsteady motions in the interacting system. In order to explore their origin, the statistical connections between the reattachment point and several signals, including the pressure fluctuations induced by the K-H vortices, the shock angle and the area of separation bubble, are investigated using the statistical quantities of coherence C_{xy} and phase θ_{xy}. The spectral coherence C_{xy} between two time signals $x(t)$ and $y(t)$ is determined as

$$C_{xy}(f) = |P_{xy}(f)|^2/(P_{xx}(f)P_{yy}(f)), \ \ 0 \leqslant C_{xy} \leqslant 1 \quad (1)$$

where P_{xx} is the power spectral density of $x(t)$ and $P_{xy}(f)$ represents the cross-power spectral density between signals $x(t)$ and $y(t)$. The phase θ_{xy} is defined as

$$\theta_{xy}(f) = \Im(P_{xy}(f))/\Re(P_{xy}(f)), \ \ -\pi < \theta_{xy} \leqslant \pi \quad (2)$$

For frequency f, if $0 < C_{xy} < 1$, it means that there is noise in the data sets or the relation between $x(t)$ and $y(t)$ is not linear. When C_{xy} equals to 1, it indicates that the signals $x(t)$ and $y(t)$ are linearly related, and $C_{xy} = 0$ means that they are completely unrelated.

First, the statistical connections between the reattachment point and separation bubble, as shown in Fig. 9, shows almost perfect correlation with each other at $f\delta_0/u_\infty \approx 0.01$ with $C \approx 0.8$, which confirms that the low frequency appears to come from the breathing motion of the separation bubble. However, there is a phase difference of $\theta \approx 1.0$ rad between these two signals. Physically, the size of the separation bubble increases when the reattachment location moves downstream.
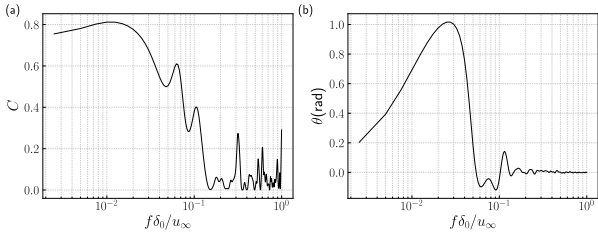
Figure 9: Statistical connections between the spanwise-averaged reattachment point and the area of separation bubble: (a) coherence and (b) phase

The coherence and phase between the spanwise-averaged reattachment point and the pressure fluctuations of the K-H vortices is shown in Fig. 10. The highest value of coherence (0.21) is observed at frequency ($f\delta_0/u_\infty \approx 0.09$), which indicates that the reattachment point and unsteadiness of K-H are slightly related around the characteristic frequency of the K-H vortices. As the the K-H vortices are located along the boundary of the separation bubble, the shear layer also shows some low-frequency features. Thereby, a second coherence peak

is found at $f\delta_0/u_\infty \approx 0.02$, around the characteristic frequency of the bubble. In terms of phase, the small absolute values manifest that these two signals are in phase over almost all of the frequency range.
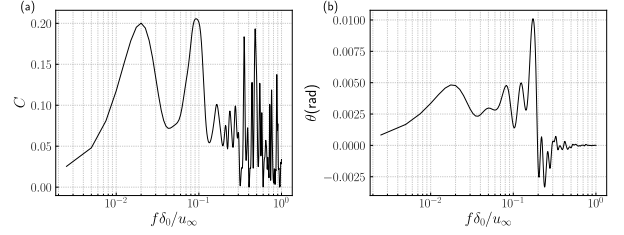
Figure 10: Statistical connections between the spanwise-averaged reattachment point and pressure fluctuations in the K-H part: (a) coherence and (b) phase

Concerning the statistical relation between the reattachment point and shock angle (Fig. 11), there are high levels of coherence ($c \approx 0.5$) at low frequency ($f\delta_0/u_\infty \approx 0.02$) and they are approximately in phase. Therefore, if the reattachment point moves downstream, the shock angle increases, and vice verse. In addition, at $f\delta_0/u_\infty \approx 0.06$, the signal of reattachment location has a certain connection to the shock angle signal, which shows that the medium-frequency unsteadiness directly associates with the oscillating behavior of the shock waves induced by the unsteady reattachment.
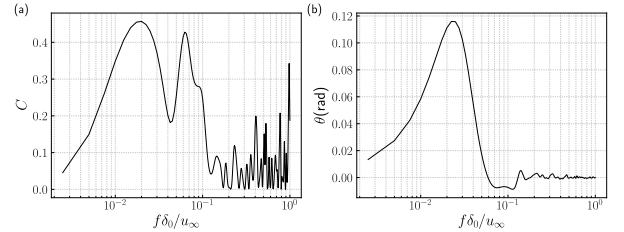
Figure 11: Statistical connections between the spanwise-averaged reattachment point and shock angle: (a) coherence and (b) phase

It should be noted that the sensitivity of the above statistical analysis to the number of samples was checked by calculating the coherence and phase with half of the total time samples. We can still get similar conclusions in spite of slight differences in frequency range due to the different resolution of frequency.

3.4 Dynamic Mode Decomposition

In order to better decouple various frequency dynamics and further validate our obtained conclusions, a modal decomposition of the flow field is carried out using a reduced-order method, dynamic mode decomposition

(DMD) [25]. Basically, given an equal-interval time series of data, DMD transforms this dynamical system into a set of dynamic modes, each of which is associated with a single orthogonal frequency behavior whose dynamics is governed by the corresponding eigenvalue. This algorithm has been widely applied for diverse flow problems, including the transition mechanism from laminar to turbulent flow [23], unsteadiness of SWBLI [8], identification of the coherent vortex structure [30], etc.

The current DMD analysis is based on 600 equal-time interval snapshots of the spanwise-averaged flow field $(tu_\infty/\delta_0 = 650 \sim 950)$ at a sample frequency $f_s\delta_0/u_\infty = 2$, which gives us a frequency resolution of $3.3 \cdot 10^{-3} < St_{\delta_0} < 1$. This leads to the normalized Frobenius norm of the residual vector with a value of 9.84×10^{-4}. In Fig. 12, we give the spectrum of eigenvalues resulting from the standard DMD. The input snapshots are real numbers while the computed modes come as complex conjugate pairs, which leads to a symmetric spectrum. The normalized Frobenius norm of the corresponding DMD modes with positive frequency are shown in Fig. 13.
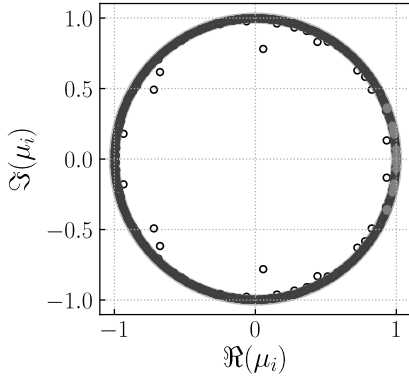

Figure 12: Eigenvalues spectrum from the standard DMD algorithm (● illustrates the most important 21 modes calculated by SPDMD).
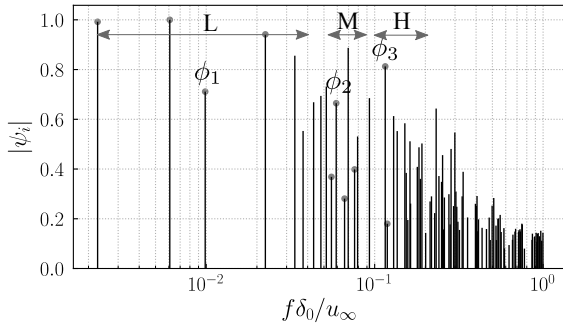

Figure 13: Normalized magnitudes of all the DMD modes with positive frequency (● illustrates the most important 10 modes calculated by SPDMD).

All these DMD modes play different roles in the whole flow field. Therefore, the sparsity-promoting dynamic mode decomposition (SPDMD) is employed to select the dynamically important modes among all the modes [12]. This method not only selects modes by their magnitudes but also picks them based on their contribution to a reproduction of the original snapshots over the given time interval. When taking the positive regularization parameter equal to 550, we obtain 10 pairs of modes with positive and negative frequency, illustrated by the gray solid circles in Fig. 12 and 13. They are considered to be the most dynamically important modes and have the most significant influence on data sequences. These modes can be categorized as three sets based on their frequency range, with $0.003 < f\delta_0/u_\infty \leqslant 0.023$, $0.055 \leqslant f\delta_0/u_\infty \leqslant 0.075$ and $0.1 < f\delta_0/u_\infty < 0.2$, respectively. These frequency ranges have been indicated in Fig. 13 and labeled as L, M and H, which stands for low, medium and high frequency. The frequencies of dominant modes are seen to be consistent with our previous statistical analysis in section 3.3.

For the branch with lower frequencies, we choose the mode with frequency $f\delta_0/u_\infty = 0.01$, marked as mode ϕ_1, to scrutinize the flow dynamics. The selected modes in the other two branches are labeled as mode ϕ_2 $(f\delta_0/u_\infty = 0.06)$ and ϕ_3 $(f\delta_0/u_\infty = 0.11)$. In Fig. 14, 15 and 16, the real and imaginary part of these modes illustrating the contour of streamwise velocity and pressure fluctuations are shown. To assist interpretation, we also reconstructed the contribution to the real-valued flow field of the individual modes by superimposing the fluctuations of each mode ϕ_i onto the mean flow ϕ_m, formulated as $q(x,t) = \phi_m + a_f \cdot \Re\{\alpha_i\phi_i e^{i\omega_i t}\}$, to examine the dynamical behavior represented by every mode, where α_i and a_f are the amplitude and optional amplification factor of the corresponding mode ϕ_i.

The low frequency mode ϕ_1 falls into the frequency of the breathing motion of separation bubble, which is the reason that high fluctuations of the streamwise velocity are distributed along the dividing line as a consequence of the flapping of the shear layer (Fig. 14a). In addition, strong pressure fluctuations are observed along the reattachment shock (Fig. 14b) due to the flapping motion of the shock wave, which is caused by the contraction and dilatation of separation bubble. Hence, we conclude that this mode involves a breathing behavior of the separation bubble and shock-wave system.

The contours of mode ϕ_2 show high levels of streamwise velocity fluctuations along the sonic line with positive and negative values distributed on the different sides (Fig. 15a), which apparently illustrates the behavior of vortex shedding initiated in the downstream section of the shear layer and starting to decay behind the reattachment. In addition, the reattachment compression and convection of shear layer vortices produce high pressure fluctuations in the supersonic part along the reattachment shock, as
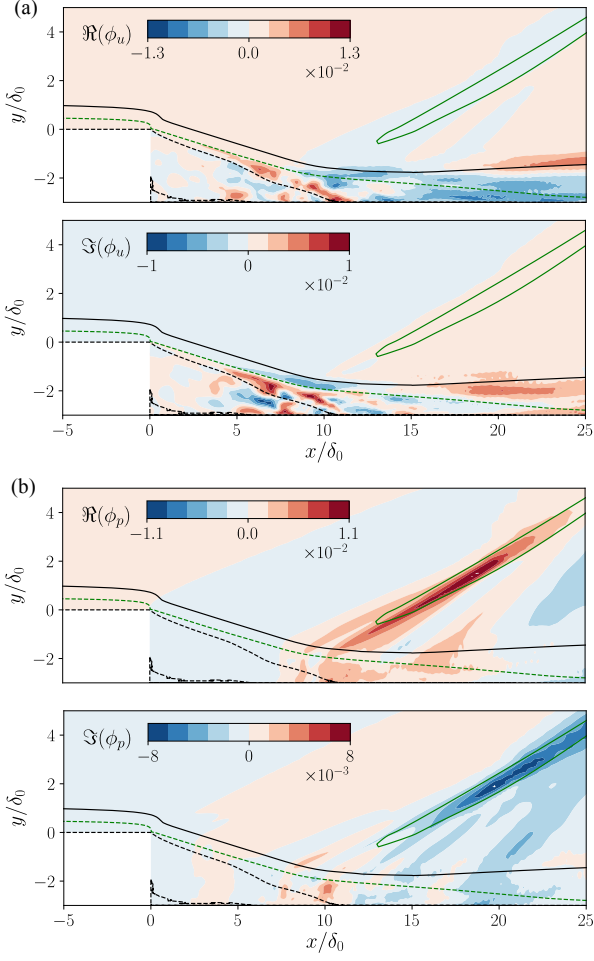
Figure 14: Real and Imaginary part of DMD mode ϕ_1 indicating contours of modal (a) streamwise velocity and (b) pressure fluctuations. The green solid and dashed line indicate the mean reattachment shock and sonic line. The black solid and dashed signify the boundary layer edge and dividing line.

Figure 15: Real and Imaginary part of DMD mode ϕ_2 indicating contours of modal (a) streamwise velocity and (b) pressure fluctuations. The green solid and dashed line indicate the mean reattachment shock and sonic line. The black solid and dashed signify the boundary layer edge and dividing line.

shown in Fig. 15b. A shock wrinkling dynamics is observed in the transient process of mode ϕ_2. The corrugation behavior of the shock is a result of the interaction between the large coherent vortices and reattaching compression. Similar results have been reported in the LES of an incident shock wave and boundary layer interactions by Pasquariello *et al.* [19].

Considering mode ϕ_3 in Fig. 16, we find alternating high positive and negative fluctuations along the streamwise direction both in streamwise velocity and pressure contour. The frequency of mode ϕ_3 is $f\delta_0/u_\infty = 0.11$, which is around the characteristic frequency of the K-H vortex based on the above-mentioned spectral analysis. The traveling of K-H vortices induce eddy Mach waves in the supersonic portion of the flow. From the temporal evolution of this mode, we can clearly see the shedding
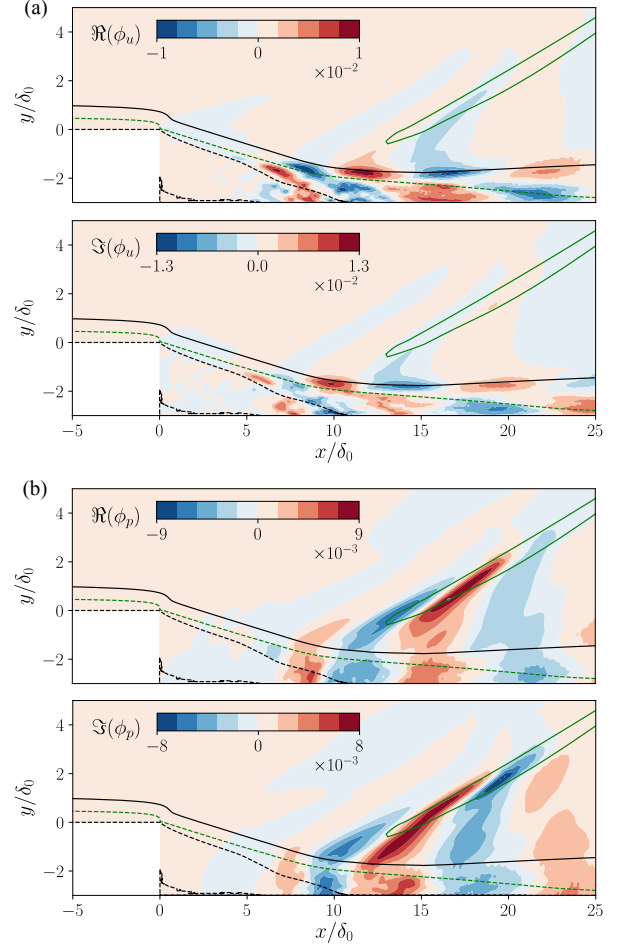
of K-H vortices with a relatively steady intensity along the streamwise direction and the convected Mach waves along the reattachment shock.

Based on the above analysis, the unsteady motions of the interacting flow contain three types of dynamics. The lower frequency branch ($0.003 < f\delta_0/u_\infty \leqslant 0.023$) describe a flow modulation that involves the breathing motion of the shock and separation bubble system. The mode ϕ_2 and ϕ_3 share similar fluctuation features while the wavelength of vortices reconstructed by ϕ_2 is visibly larger than that of vortices represented by ϕ_3. Considering their frequencies, in addition, we believe the medium-frequency (centered at $f\delta_0/u_\infty = 0.06$) modes relates to the large vortex decaying and reattaching compression; while the higher-frequency part (around K-H vortices characteristic frequency $f\delta_0/u_\infty = 0.11$) is associated with the convection of K-H vortices and induced
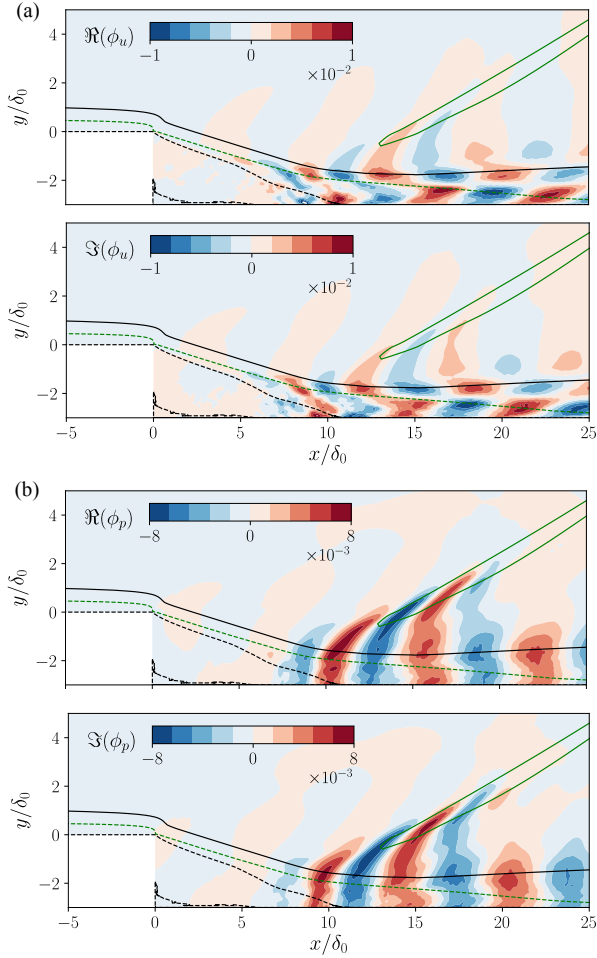
(a)
$\Re(\phi_u)$

$\Im(\phi_u)$

(b)
$\Re(\phi_p)$

$\Im(\phi_p)$

Figure 16: Real and Imaginary part of DMD mode ϕ_3 indicating contours of modal (a) streamwise velocity and (b) pressure fluctuations. The green solid and dashed line indicate the mean reattachment shock and sonic line. The black solid and dashed signify the boundary layer edge and dividing line.

Mach waves.

4. DISCUSSION

The spectral analysis shows that there is a broad band of oscillations with three branches of dominant frequency centered near $f\delta_0/u_\infty = 0.01, 0.06, 0.1$ in the current case. Their unsteady interactions can be classified as two different patterns according to the shape of separation bubble, namely expansion and collapse. In the dilatation process of separation bubble, the reattachment point and shock location moves downstream, as shown in the schematic Fig. 17. In the phase of collapsing, the reattachment location has a sudden drop and new K-H vortices appear at the beginning of the separated shear layer, while the shock angle smoothly decreases. The

motions of shock and separation bubble is not symmetric in terms of the amplitude and slope. The variation of these parameters are addressed in the section of spectral and statistical analysis. In addition, the animations of reconstructing flow from DMD modes also elucidate these features of the flow field.
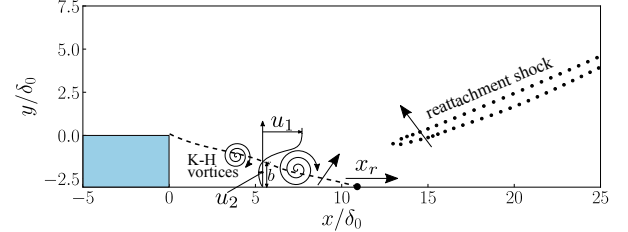

Figure 17: Pattern of the separation bubble dilatation. The dashed line denotes the dividing line.

The mechanism of this unsteady behavior can be explained by the theory of Piponniau *et al.* [20]. This simplified model relates the low-frequency unsteadiness of shock and separation bubble to the fluid entrainment in the shear layer. The dilation of the bubble is associated with a continuous entrainment of mass flux, while the collapse corresponds to a radical expulsion of the mass entrained in the bubble. As shown in Fig. 17, the midpoint of the mean reattachment length is taken as the reference location to estimate the spreading rate. The height of the intersection between the reference line and dividing line is marked as b. The locations 1 and 2 are situated at the positions with maximum and minimum streamwise velocity respectively.

The spreading rate of the mixing layer not only depends upon the velocity ratio $r = u_2/u_1$ and density ratio $s = \rho_2/\rho_1$ across the mixing layer [1] but also strongly relate to compressibility effects [18], which depends on the isentropic convective Mach number M_c, defined by

$$M_c = \frac{\Delta U}{a_1 + a_2} \qquad (3)$$

where a_i denotes the sound velocity, ΔU is the velocity difference between two locations. Then the characteristic frequency of the unsteadiness can be formulated as a function of r, s and M_c,

$$S_b = fb/u_1 = \Phi(M_c)g(r,s) \qquad (4)$$

where $g(r,s)$ can be approximated by

$$g(r,s) = \frac{b'}{2}\frac{(1-r)(1+\sqrt{s})}{1+r\sqrt{s}}[(1-r)C+\frac{r}{2}] \qquad (5)$$

The constant $C \approx 0.14$ is estimated by the similarity function and b' is the slope of dividing line at the reference location, approximated by $b' = b/x$. The function of the normalized spreading rate $\Phi(M_c)$ is given as a curve by

Smits & Dussauge [26]. Using this model, we calculate all the involved parameters of the current numerical results, given in Tab. 2 and we convert S_b to S_{δ_0} based on the reference length δ_0 and velocity u_∞:

$$S_{\delta_0} = S_b \frac{u_1}{b} \frac{\delta_0}{u_\infty} \qquad (6)$$

We finally obtain $S_{\delta_0} = 0.007$, which falls in the first branch of DMD modes representing shock motions.

Table 2: Aerodynamic variables of the interacting system and the corresponding Strouhal number of reattachment shock computed from Equ. 4.

b/δ_0	x/δ_0	a_1/u_∞	a_2/u_∞	u_1/u_∞	u_2/u_∞
1.64	5.45	0.5324	0.7082	1.1180	-0.0415
M_c	$\Phi(M_c)$	ρ_1/ρ_∞	ρ_2/ρ_∞	$g(r,s)$	S_b
0.9346	0.29	0.6041	0.3402	0.0356	0.0103

5. CONCLUSIONS

We numerically investigated the unsteady behavior of shock wave-boundary layer interactions in a transitional BFS flow at $Ma = 1.7$ and $Re_{\delta_0} = 13718$. The unsteadiness of the interaction system is characterized by a modulation of a broadband frequency dynamics. The breathing behavior of the separation bubble and shock is associated with a lower frequency centered at $f\delta_0/u_\infty = 0.01$. This unsteadiness is caused by the periodical fluid entrainment of the shear layer (collapse of the bubble) and reinjection of the low-speed reverse flow (expansion of the bubble). The frequency of the shock motion can also be validated by the simple model proposed by Piponniau *et al.* [20]. The medium frequency mode is associated to the large coherent vortex shedding in the shear layer and the wrinkling behavior of the shock, while the higher frequency mode is related to the traveling of K-H vortices and induced Mach waves.

REFERENCES

[1] G. L. Brown and A. Roshko. On density effects and large structure in turbulent mixing layers. *J. Fluid Mech.*, 64(4):775–816, 1974.

[2] N. T. Clemens and V. Narayanaswamy. Low-Frequency Unsteadiness of Shock Wave/Turbulent Boundary Layer Interactions. *Annu. Rev. Fluid Mech.*, 46:469–492, 2014.

[3] J. Délery, J. G. Marvin, and E. Reshotko. Shock-wave boundary layer interactions. Technical report, DTIC Document, 1986.

[4] D. S. Dolling. Fifty years of shock-wave/boundary-layer interaction research - What next? *AIAA J.*, 39(8):1517–1531, 2001.

[5] D. V. Gaitonde. Progress in shock wave/boundary layer interactions. *Prog. Aerosp. Sci.*, 72:80–99, 2015.

[6] S. Gottlieb and C.-W. Shu. Total variation diminishing Runge-Kutta schemes. Technical Report 98, 1998.

[7] J. E. Green. Interactions between shock waves and turbulent boundary layers. *Prog. Aerosp. Sci.*, 11:235–340, 1970.

[8] M. Grilli, P. J. Schmid, S. Hickel, and N. A. Adams. Analysis of unsteady behaviour in shockwave turbulent boundary layer interaction. *J. Fluid Mech.*, 700:16–28, 2012.

[9] F. Guiho, F. Alizard, and J. C. Robinet. Instabilities in oblique shock wave/laminar boundary-layer interactions. *J. Fluid Mech.*, 789:1–35, 2016.

[10] S. Hickel, N. A. Adams, and J. A. Domaradzki. An adaptive local deconvolution method for implicit LES. *J. Comput. Phys.*, 213(1):413–436, 2006.

[11] S. Hickel, C. P. Egerer, and J. Larsson. Subgrid-scale modeling for implicit large eddy simulation of compressible flows and shock-turbulence interaction. *Phys. Fluids*, 26(10):106101, 2014.

[12] M. R. Jovanović, P. J. Schmid, and J. W. Nichols. Sparsity-promoting dynamic mode decomposition. *Phys. Fluids*, 26(2):024103, 2014.

[13] A. Karimi, S. Wijeyakulasuriya, and M. Nalim. Numerical Study of Supersonic Flow over Backward-Facing Step for Scramjet Application. In *48th AIAA/ASME/SAE/ASEE Jt. Propuls. Conf. Exhib.*, Reston, Virigina, 2012. American Institute of Aeronautics and Astronautics.

[14] I. Lee and H. J. Sung. Multiple-arrayed pressure measurement for investigation of the unsteady flow structure of a reattaching shear layer. *J. Fluid Mech.*, 463:377–402, 2002.

[15] H. Liu, B. Wang, Y. Guo, H. Zhang, and W. Lin. Effects of Inflow Mach Number and Step Height on Supersonic Flows over a Backward-Facing Step. *Adv. Mech. Eng.*, 5:147916, 2013.

[16] J. Matheis and S. Hickel. On the transition between regular and irregular shock patterns of shock-wave/boundary-layer interactions. *J. Fluid Mech.*, 776:200–234, 2015.

[17] Y. Na and P. Moin. Direct numerical simulation of a separated turbulent boundary layer. *J. Fluid Mech.*, 374:379–405, 1998.

[18] D. Papamoschou and A. Roshko. The compressible turbulent shear layer: an experimental study. *J. Fluid Mech.*, 197:453–477, 1988.

[19] V. Pasquariello, S. Hickel, and N. A. Adams. Unsteady effects of strong shock-wave/boundary-layer interaction at high Reynolds number. *J. Fluid Mech.*, 823:617–657, 2017.

[20] S. Piponniau, J. P. Dussauge, J. F. Debiève, and P. Dupont. A simple model for low-frequency unsteadiness in shock-induced separation. *J. Fluid Mech.*, 629:87, 2009.

[21] S. Priebe and M. P. Martín. Low-frequency unsteadiness in shock wave–turbulent boundary layer interaction. *J. Fluid Mech.*, 699:1–49, 2012.

[22] S. Priebe, J. H. Tu, C. W. Rowley, and M. P. Martín. Low-frequency dynamics in a shock-induced separated flow. *J. Fluid Mech.*, 807:441–477, 2016.

[23] B. T. Sayadi, P. Schmid, J. W. Nichols, and P. Moin. Dynamic mode decomposition of controlled H-and K-type transitions. *Cent. Turbul. Res. Annu. Res. Briefs*, pages 189–200, 2013.

[24] F. Schäfer, M. Breuer, and F. Durst. The dynamics of the transitional flow over a backward-facing step. *J. Fluid Mech.*, 623:85, 2009.

[25] P. J. Schmid. Dynamic mode decomposition of numerical and experimental data. *J. Fluid Mech.*, 656:5–28, 2010.

[26] A. J. Smits and J. P. Dussauge. *Turbulent Shear Layers in Supersonic Flow*. *Springer Science & Business Media*, 2006.

[27] P. G. Spazzini, G. Iuso, M. Onorato, N. Zurlo, and G. M. Di Cicca. Unsteady behavior of back-facing step flow. *Exp. Fluids*, 30(5):551–561, 2001.

[28] Z. Sun, F. Schrijer, and B. Van Oudheusden. PIV Investigation of the 3D instantaneous flow organization behind a micro-ramp in a supersonic boundary layer. *28th Int. Symp. Shock Waves*, 2:417–423, 2012.

[29] Y. Yan and C. Liu. Study on the ring-like vortical structure in MVG controlled supersonic ramp flow with different inflow conditions. *Aerosp. Sci. Technol.*, 35:106–115, 2014.

[30] Q. Zhang, Y. Liu, and S. Wang. The identification of coherent structures using proper orthogonal decomposition and dynamic mode decomposition. *J. Fluids Struct.*, 49:53–72, 2014.

[31] Y. Zhu, S. Yi, D. Gang, and L. He. Visualisation on supersonic flow over backward-facing step with or without roughness. *J. Turbul.*, 16(7):633–649, 2015.